Optics Letters

Flatband mode in photonic moiré superlattice for boosting second-harmonic generation with monolayer van der Waals crystals

Peilong Hong,[1,3] Lei Xu,[2,4] Cuifeng Ying,[2] and Mohsen Rahmani[2]

[1]School of Optoelectronic Science and Engineering, University of Electronic Science and Technology of China (UESTC), Chengdu 611731, China
[2]Advanced Optics & Photonics Laboratory, Department of Engineering, School of Science & Technology, Nottingham Trent University, Nottingham NG11 8NS, UK
[3]e-mail: plhong@uestc.edu.cn
[4]e-mail: lei.xu@ntu.ac.uk

Received 14 January 2022; revised 3 March 2022; accepted 22 March 2022; posted 25 March 2022; published 26 April 2022

We theoretically investigate boosting second-harmonic generation (SHG) of monolayer van der Waals crystals by employing flatband modes hosted by photonic moiré superlattices. Such a system with high quality factor and a monolayer crystal accommodated on the top of it, provides a unique opportunity to enhance and manipulate SHG emission. We show that employing a doubly resonant diagram on such a moiré superlattice system not only boosts the SHG, but also tunes the directional emission of the second-harmonic wave. Moreover, we demonstrate that a structured beam illumination could further boost SHG, with the phase structure retrieved through a two-beam second-harmonic interference configuration. These results suggest the flatband modes in moiré superlattice as a promising platform for boosting SHG with monolayer van der Waals crystals, offering new possibilities for developing compact nonlinear photonic devices.

© 2022 Optica Publishing Group under the terms of the Optica Open Access Publishing Agreement

https://doi.org/10.1364/OL.453625

Moiré fringes or moiré patterns emerge when superposing two slightly different periodical patterns. The moiré superlattices host exotic electronic states in condensed-matter systems, leading to many salient physical phenomena, such as magic-angle graphene [1], moiré excitons [2], fractional Chern insulator [3], etc. By employing the correspondence between electronic waves and light waves, a surge of effort has been devoted recently to exploring moiré physics in optics [4–13], showing promising breakthroughs both fundamentally and practically. The flatbands hosted by moiré superlattices is a remarkable feature that can be achieved by tuning the twisting angles ("magic angles" [12]), as well as by scanning the separations between the bilayer photonic slabs ("magic distances" [14]). The flatbands has been reported in mismatched hexagonal-lattice metacrystals [10], twisted bilayer honeycomb photonic crystals [7,12], and mismatched bilayer 1D photonic crystal slabs [14]. These flatbands are related to localized modes in moiré superlattices, and therefore are of great interest for enhancing light–matter interactions, such as lasing and optical nonlinear processes.

In nonlinear optics, second-harmonic generation (SHG) is a widespread method for coherently manipulating the wavelength of light, key for applications such as light-source generation, imaging, and sensing [15]. Recently, SHG with monolayer van der Waals crystals has received a lot of interest, since these 2D material monolayers offer remarkable optical features such as room-temperature stable excitons [16], optical chiral responsivity [17–20], and large and tunable nonlinear susceptibility [21–27]. However, due to their sub-nanometer thickness, monolayer van der Waals crystals unavoidably exhibit low SHG efficiency. There is a high demand for boosting the SHG of 2D material monolayers. Several pioneer works have demonstrated enhanced SHG with plasmonic resonant structures [18,28–30], optical waveguides [31], dielectric metasurfaces [32,33], photonic crystals [34–36], nanowires [37], topological photonic crystals [38–40], etc.

This work concerns a theoretical study of boosting the SHG of monolayer van der Waals crystals with flatband modes in a moiré superlattice. We show that merely with a single isolated cell of the moiré superlattice, the flatband mode exhibits high quality factor, and thus could significantly boost the SHG of monolayer van der Waals crystals. Notably, we have considered a flatband mode relatively stable against a change of the thickness of the slabs. This feature makes it possible to tailor a doubly resonant diagram for further enhancing the SHG, as well as tuning the directional emission of the second-harmonic wave (SHW). The SHG enhancement is found to be dependent on the incident angle of the fundamental wave (FW), due to the complex far-field features of the flatband mode. Moreover, it is shown that structured beam illumination with the phase structure obtained from two-beam second-harmonic interference can further boost the SHG. These results open new possibilities for SHG with monolayer van der Waals crystals based on photonic moiré superlattices.

We consider a mismatched bilayer silicon photonic system, with each layer being a 1D photonic crystal slab as shown in

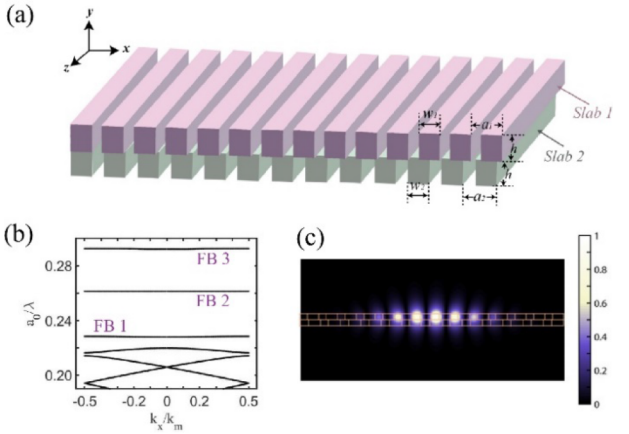

Fig. 1. (a) Moiré superlattice via stacked bilayer photonic crystal slabs. (b) Band structure of the moiré superlattice with $h = 0.3a_0$. Here, $k_m = 2\pi/a_M$. (c) Field distribution of the FB 2 mode at $k_x = 0$ with $h = 0.3a_0$.

Fig. 1. The unit cell size is a_1 for the top slab (Slab 1) and a_2 for the bottom slab (Slab 2). The width of the dielectric strip is set to be $w_j = g_w\, a_j$ $(j = 1,\ 2)$, with g_w fixed at 0.4. The size of the moiré superlattice is $a_M = Na_1 = (N-1)\, a_2$ for the commensurate configuration. Without losing generality, the integer N is fixed to be 14 here. The thickness of both photonic slabs is set as $h = g_h\, a_0$, with $a_0 = (a_1 + a_2)/2$. By tuning h, the interlayer coupling of the bilayer system changes accordingly, leading to flatbands at different eigenfrequencies. Figure 1(b) shows the band structure of the superlattice with $h = 0.3a_0$, where the three lowest flatbands are marked. Here, we focus on the FB 2 mode that resides mostly in the top slab [Fig. 1(c)], and is more tightly confined compared with FB 1 and FB 3 modes (see details in Sect. 1 of Supplement 1). Due to the flatband nature, the FB 2 mode can be hosted in a single isolated cell of the moiré superlattice, showing high quality factor Q up to 70,000 [see Fig. S3(a) in Supplement 1], and thus offers the possibility of enhancing the SHG of monolayer van de Waals crystals.

Here, a WS_2 monolayer (thickness ~ 0.618 nm) is considered to be placed on the top of Slab 1, as shown in the inset of Fig. 2(a). The armchair crystal direction of WS_2 is aligned along the z axis (parallel to the silicon strip), the same as the polarization direction of the FW. Consequently, the effective nonlinear susceptibility of the WS_2 monolayer is $\chi^{(2)}_{zzz}$ [20,41], giving rise to second-order polarizability as

$$P_z^{(2)}\left(2\omega,\ \vec{r}\right) = \varepsilon_0\, \chi^{(2)}_{zzz} \cdot E_z\left(\omega,\ \vec{r}\right) E_z\left(\omega,\ \vec{r}\right), \qquad (1)$$

where $E_z\left(\omega,\ \vec{r}\right)$ denotes the electric field of the FW and ε_0 is the vacuum permittivity. This configuration leads to a second-harmonic emission with the same polarization as the FW. The nonlinear susceptibility of the WS_2 monolayer $\chi^{(2)}_{zzz}$ is set as 100 pm/V in the full-wave simulation. Additionally, we consider the SHG for converting a ~1560 nm FW to a ~780 nm SHW. The refractive index of the WS_2 monolayer is set as 3.48 + 0.08i at ~1560 nm and 3.85 + 0.20i at ~780 nm [42]. The refractive index for the silicon is set as 3.47 at ~1560 nm [43] and 3.7 + 0.006i at ~780 nm [44]. After placing the WS_2 monolayer, the absorptive WS_2 monolayer decreases the quality factor Q of the flatband mode [Fig. 2(a)]. Nonetheless, the flatband mode keeps the localization feature [see Fig. S3(c) in Supplement 1].

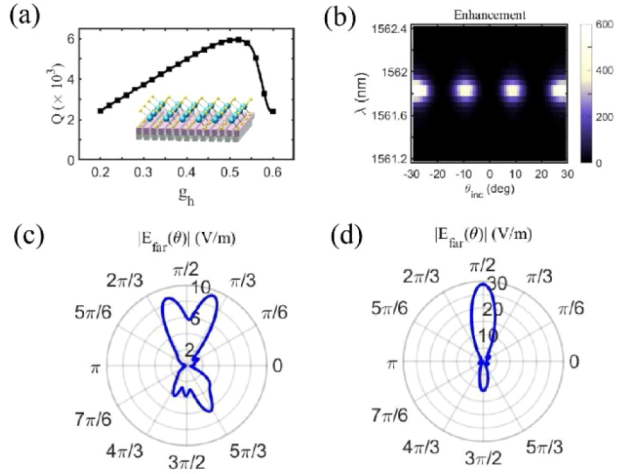

Fig. 2. (a) Quality factor Q of the FB 2 mode, with WS_2 monolayer accommodated on top of the moiré superlattice. The line is a guide for the eye. (b) Enhancement of SHG with slab thickness $h = 0.5a_0$. (c) Far-field distribution of the SHW $|E_{far}(\theta)|$ with incident angle of the FW at 9° ($h = 0.5a_0$). (d) Far-field emission patterns of the SHW $|E_{far}(\theta)|$ with the excitation light incident at an angle of 9° (doubly resonant diagram with $h = 0.365a_0$).

For SHG, we considered a quasi-plane beam for exciting the WS_2 monolayer [see Fig. S4(a) in Supplement 1], with the width of the incident angle of 2° and intensity of 0.1 GW/cm^2. At the normal incidence with the same quasi-plane FW, a free-standing WS_2 monolayer gives a constant SHG efficiency $P_{2\omega}/P_{\omega} = 0.445 \times 10^{-10}$ within the spectral range of interest. Here the full-wave simulation is done with undepleted pump approximation. In the moiré superlattice configuration (slab thickness $h = 0.5a_0$ and $a_M = 4.8\ \mu$m), we scanned the incident angle of the quasi-plane FW from −29° to 29° at a step of 2° in the xy plane, and monitored the total power of the SHW in the far-field domain within [−30°, 30°]. The SHG efficiency is calculated with the power of the FW at normal incidence, and the enhancement of SHG [Fig. 2(b)] is obtained by dividing the SHG efficiency of a free-standing WS_2 monolayer. The enhancement is dependent on the incident angle and the wavelength of the excitation light. At resonant excitation with 1561.8 nm FW, the SHG is significantly enhanced at several incident angles. This incident angle dependence is related to the complex far-field pattern of the flatband mode [see Fig. S3(b) in Supplement 1]. The maximum enhancement factor is around 600 within the scan range, indicating that the SHG efficiency is enhanced up to 2.67×10^{-8}. The near-field distribution of the SHW can be found in Fig. S4(b) in Supplement 1. Besides, the far-field emission pattern shown in Fig. 2(c) indicates the emission directionality of the SHW, which originates from the interaction between the nonlinear polarization of WS_2 and the moiré superlattice.

Since the FB 2 mode keeps a high Q while scanning the thickness of the moiré superlattice [Fig. 2(a)], this feature enables us to design a doubly resonant diagram for further boosting SHG. To achieve resonances at both the fundamental and harmonic waves, we have checked the eigenmodes with eigenfrequencies near twice that of the FW. Particularly, we focused on the eigenmodes with a strong directional far-field lobe along the y axis. With these considerations, we found that the case with a slab thickness of $0.365a_0$ ($a_M = 5.2$ µm) fulfills the doubly resonant condition when the wavelength of the FW is 1560.1 nm. The

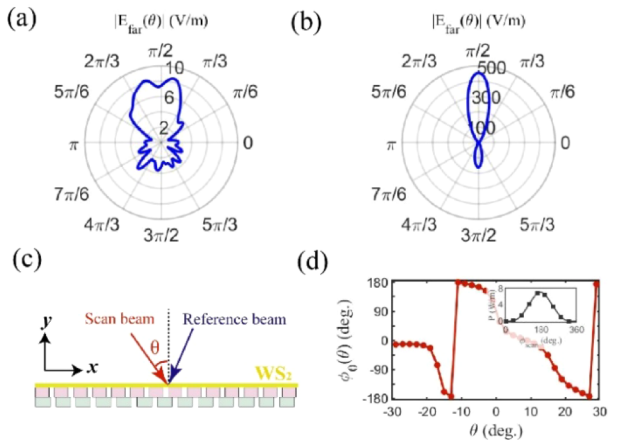

Fig. 3. Far-field emission pattern in (a) the focused beam configuration and (b) the structured beam configuration. Here, $h = 0.365a_0$. (c) Two-beam second-harmonic interference diagram for phase retrieval. (d) Retrieved phase $\varphi_0(\theta)$ for the whole scan range. The inset shows a fitting curve ($\theta_{\text{ref}} = 9°$ and $\theta = -9°$) using Eq. (3) in the phase retrieval process.

quality factor for the SHW resonant eigenmode is 16.5, and its far-field patterns can be found in Fig. S5(a) in Supplement 1. We did a full-wave simulation to get the SHG efficiency versus the incident angle, with other settings the same as above. The maximum enhancement is larger than 3000 [see Fig. S5(b) in Supplement 1], and is higher than that with a thickness of $0.5a_0$, although the quality factor of the flatband mode is lower than that with $0.5a_0$ shown in Fig. 2(a). In addition to this pronounced enhancement, the doubly resonant diagram leads to a more directional emission of the SHW shown in Fig. 2(d), indicating the possibility of controlling the directional emission of the SHW. This result has been further confirmed with another doubly resonant diagram (see Fig. S6 in Supplement 1).

To excite the flatband mode in a finite-size moiré superlattice (here for a single isolated cell), a spatially confined beam could be more efficient than a plane wave. To investigate the focus configuration for enhancing SHG, we considered a doubly resonant diagram with $h = 0.365a_0$. The focused beam is built by superposing plane waves with θ_{inc} in the range $[-30°, 30°]$, and with the same total power as the quasi-plane wave. Again, all other settings are kept the same as above. We obtained a SHG enhancement of 344 with the focused beam excitation, which is not high compared with that obtained with quasi-plane-wave excitation (~3000). Therefore, simply sending a focused beam to the moiré superlattice does not necessarily improve the SHG efficiency. The reason lies in the fact that different plane waves may lead to destructive excitation of the flatband mode, due to the complex far-field pattern of the flatband mode [Fig. S3(b) in Supplement 1]. Besides, the far-field emission pattern of the SHW [Fig. 3(a)] exhibits less directionality as compared with that excited with the quasi-plane wave [Fig. 2(d)].

To circumvent this issue, we propose a two-beam second-harmonic interference configuration [Fig. 3(c)] for generating a structured incident beam. The structured beam leads to constructive excitation of the flatband mode with multiple plane waves incident from different angles. In this case, we kept the total power of the structured beam the same as that of the focused beam, and obtained a SHG enhancement of 5.4×10^5, much higher than the enhancement in the focused beam case. The far-field emission pattern of the SHW is shown in Fig. 3(b), indicating that the directional emission is recovered compared with the focused beam case.

To get the phases for structured beam illumination, we numerically implemented a phase retrieval procedure based on two-beam second-harmonic interference schematically shown in Fig. 3(c). This phase retrieval process can also be implemented experimentally with an interferometer or with a spatial light modulator placed at the Fourier plane of the moiré superlattice. In the two-beam configuration, the first plane wave at an angle θ_{ref} is used as a reference beam, the phase of which keeps unchanged. On the contrary, the phase of the plane wave at angle θ is scanned equidistantly as $\{0, 2\pi/9, \ldots, 16\pi/9\}$. Simultaneously, the intensity of the SHW emitted to the far field is monitored within the angle range of $[-30°, 30°]$. Theoretically, the SHW intensity is proportional to the superposition probability of the nonlinear two-photon amplitudes at the WS_2 monolayer, expressed as

$$I_{2\omega} \propto \left| \begin{array}{c} A_{\text{ref}} \cdot A_{\text{ref}} + A_{\text{scan}}(\theta)e^{j\varphi_{\text{scan}}} \cdot A_{\text{scan}}(\theta)e^{j\varphi_{\text{scan}}} \\ +2A_{\text{ref}} \cdot \ A_{\text{scan}}(\theta)e^{j\varphi_{\text{scan}}} \end{array} \right|^2. \quad (2)$$

Here, A_{ref} denotes the complex amplitude of the flatband mode that is excited by the reference wave while $A_{\text{scan}}(\theta)$ denotes the complex amplitude excited by the scanning wave. Phase φ_{scan} is the modulating phase loaded on the scan wave. Equation (2) can be rewritten as

$$\begin{aligned} I_{2\omega} \propto \ & B_0 + B_1 \cos(\varphi_{\text{scan}} + \varphi_0(\theta)) \\ & + B_2 \cos(2\varphi_{\text{scan}} + 2\varphi_0(\theta)), \end{aligned} \quad (3)$$

where $\varphi_0(\theta)$ is the phase difference between the two complex amplitudes A_{ref} and $A_{\text{scan}}(\theta)$, $B_0 = |A_{\text{ref}}|^4 + |A_{\text{scan}}|^4 + 4|A_{\text{ref}}|^2|A_{\text{scan}}|^2$, $B_1 = 4|A_{\text{ref}}|^3|A_{\text{scan}}| + 4|A_{\text{ref}}||A_{\text{scan}}|^3$, and $B_2 = 2|A_{\text{ref}}|^2|A_{\text{scan}}|^2$. By employing Eq. (3) for fitting the two-beam second-harmonic interference results, one can get the phase $\varphi_0(\theta)$ for each scan beam. An example fitting result is shown in the inset of Fig. 3(d), together with the full-wave simulation data points. The overall retrieved phases at different scan angles are shown in Fig. 3(d). With the retrieved phases $\varphi_0(\theta)$, $-\varphi_0(\theta)$ are loaded on the multiple incident plane waves at different angles θ within $[-30°, 30°]$, generating a structured beam incident on the isolated cell of the superlattice. This structured beam then constructively excites the highly confined flatband mode, responsible for the enhanced SHG and the directional emission of the SHW shown in Fig. 3(b).

We note that the separation between the two photonic slabs may affect the quality factor Q of the flatband mode, and a detailed exploration can be found in Fig. S7 in Supplement 1. Generally, by significantly changing the separation, the appearance and disappearance of the flatbands will be observed in moiré superlattices [12,14], indicating the separation and the thickness of the photonic slabs can be jointly tuned for obtaining the flatband modes. Moreover, the 2D monolayer can also be located at different interfaces of the moiré superlattice, as long as there is sufficient overlap between the 2D monolayer and the flatband mode. The change of the location of the 2D monolayer could lead to a change of the second-harmonic emission, since the optical path of the emitted SHW has also changed. Certainly, the moiré superlattices could be constructed by using other kinds of slightly mismatched 1D or 2D periodical photonic structures [7,10,12,14]. By tuning the structural parameters such as the thickness, the separation, and the rotation angles, the flatbands

can be obtained, offering flexible choices for different practical situations. Our work on SHG may provide a first attempt to exploit these intriguing modes to empower nonlinear optics.

In conclusion, we have theoretically demonstrated that the flatband hosted by a moiré superlattice can be a valuable resource for boosting SHG with monolayer van der Waals crystals. The quality factor of the flatband mode is limited by the absorption coefficient of the WS_2 monolayer but still leads to enhanced SHG by a factor >600 with plane-wave excitation. Besides, a doubly resonant diagram is investigated which not only further boosts SHG but also controls the directionality of the second harmonic emission. Moreover, a two-beam second-harmonic interference is proposed for generating a structured beam for exciting the moiré superlattice, such that the SHG is enhanced up to 5.4×10^5 times. Our results show the promising potential of moiré flatbands for boosting SHG, opening new possibilities for exploring moiré photonics in nonlinear optics.

Funding. Fundamental Research Funds for the Central Universities (ZYGX2020J010); UK Research and Innovation (MR/T040513/1).

Acknowledgment. P.H. is grateful for the support of the Fundamental Research Funds for the Central Universities (ZYGX2020J010). M.R. and L.X. appreciate support from the UK Research and Innovation Future Leaders Fellowship (MR/T040513/1).

Disclosures. The authors declare no conflicts of interest.

Data availability. Data underlying the results presented in this paper are not publicly available at this time but may be obtained from the authors upon reasonable request.

Supplemental document. See Supplement 1 for supporting content.

REFERENCES

1. Y. Cao, V. Fatemi, S. Fang, K. Watanabe, T. Taniguchi, E. Kaxiras, and P. Jarillo-Herrero, Nature **556**, 43 (2018).
2. K. Tran, G. Moody, and F. Wu, *et al.*, Nature **567**, 71 (2019).
3. A. Abouelkomsan, Z. Liu, and E. J. Bergholtz, Phys. Rev. Lett. **124**, 106803 (2020).
4. G. Hu, A. Krasnok, Y. Mazor, C.-W. Qiu, and A. Alù, Nano Lett. **20**, 3217 (2020).
5. G. Hu, Q. Ou, G. Si, Y. Wu, J. Wu, Z. Dai, A. Krasnok, Y. Mazor, Q. Zhang, Q. Bao, C.-W. Qiu, and A. Alù, Nature **582**, 209 (2020).
6. B. Lou, N. Zhao, M. Minkov, C. Guo, M. Orenstein, and S. Fan, Phys. Rev. Lett. **126**, 136101 (2021).
7. X.-R. Mao, Z.-K. Shao, H.-Y. Luan, S.-L. Wang, and R.-M. Ma, Nat. Nanotechnol. **16**, 1099 (2021).
8. S. S. Sunku, G. X. Ni, B. Y. Jiang, H. Yoo, A. Sternbach, A. S. McLeod, T. Stauber, L. Xiong, T. Taniguchi, K. Watanabe, P. Kim, M. M. Fogler, and D. N. Basov, Science **362**, 1153 (2018).
9. P. Wang, Y. Zheng, X. Chen, C. Huang, Y. V. Kartashov, L. Torner, V. V. Konotop, and F. Ye, Nature **577**, 42 (2020).
10. W. Wang, W. Gao, X. Chen, F. Shi, G. Li, J. Dong, Y. Xiang, and S. Zhang, Phys. Rev. Lett. **125**, 203901 (2020).
11. Z. Wu, X. Chen, M. Wang, J. Dong, and Y. Zheng, ACS Nano **12**, 5030 (2018).
12. K. Dong, T. Zhang, J. Li, Q. Wang, F. Yang, Y. Rho, D. Wang, C. P. Grigoropoulos, J. Wu, and J. Yao, Phys. Rev. Lett. **126**, 223601 (2021).
13. Q. Fu, P. Wang, C. Huang, Y. V. Kartashov, L. Torner, V. V. Konotop, and F. Ye, Nat. Photonics **14**, 663 (2020).
14. D. X. Nguyen, X. Letartre, E. Drouard, P. Viktorovitch, H. C. Nguyen, and H. S. Nguyen, "Magic configurations in moiré superlattice of bilayer photonic crystal: almost-perfect flatbands and unconventional localization," arXiv:2104.12774 (2021).
15. M. Rahmani, G. Leo, I. Brener, A. V. Zayats, S. A. Maier, C. De Angelis, H. Tan, V. F. Gili, F. Karouta, R. Oulton, K. Vora, M. Lysevych, I. Staude, L. Xu, A. E. Miroshnichenko, C. Jagadish, and D. N. Neshev, Opto-Electron. Adv. **1**, 18002101 (2018).
16. L. Hayen, N. Severijns, K. Bodek, D. Rozpedzik, and X. Mougeot, Rev. Mod. Phys. **90**, 015008 (2018).
17. L. Mouchliadis, S. Psilodimitrakopoulos, G. M. Maragkakis, I. Demeridou, G. Kourmoulakis, A. Lemonis, G. Kioseoglou, and E. Stratakis, npj 2D Mater. Appl. **5**, 6 (2021).
18. G. Hu, X. Hong, K. Wang, J. Wu, H.-X. Xu, W. Zhao, W. Liu, S. Zhang, F. Garcia-Vidal, B. Wang, P. Lu, and C.-W. Qiu, Nat. Photonics **13**, 467 (2019).
19. D. Zhang, Z. Zeng, Q. Tong, Y. Jiang, S. Chen, B. Zheng, J. Qu, F. Li, W. Zheng, F. Jiang, H. Zhao, L. Huang, K. Braun, A. J. Meixner, X. Wang, and A. Pan, Adv. Mater. **32**, 1908061 (2020).
20. G. Miltos Maragkakis, S. Psilodimitrakopoulos, L. Mouchliadis, I. Paradisanos, A. Lemonis, G. Kioseoglou, and E. Stratakis, Opto-Electron. Adv. **2**, 19002601 (2019).
21. N. Kumar, S. Najmaei, Q. Cui, F. Ceballos, P. M. Ajayan, J. Lou, and H. Zhao, Phys. Rev. B **87**, 161403 (2013).
22. L. M. Malard, T. V. Alencar, A. P. M. Barboza, K. F. Mak, and A. M. de Paula, Phys. Rev. B **87**, 201401 (2013).
23. C. Janisch, Y. Wang, D. Ma, N. Mehta, A. L. Elías, N. Perea-López, M. Terrones, V. Crespi, and Z. Liu, Sci. Rep. **4**, 5530 (2015).
24. K. L. Seyler, J. R. Schaibley, P. Gong, P. Rivera, A. M. Jones, S. Wu, J. Yan, D. G. Mandrus, W. Yao, and X. Xu, Nat. Nanotechnol. **10**, 407 (2015).
25. X. Zhou, J. Cheng, Y. Zhou, T. Cao, H. Hong, Z. Liao, S. Wu, H. Peng, K. Liu, and D. Yu, J. Am. Chem. Soc. **137**, 7994 (2015).
26. L. Mennel, M. Paur, and T. Mueller, APL Photonics **4**, 034404 (2019).
27. M. Liu, H. Wu, X. Liu, Y. Wang, M. Lei, W. Liu, W. Guo, and Z. Wei, Opto-Electron. Adv. **4**, 200029 (2021).
28. Z. Wang, Z. Dong, H. Zhu, L. Jin, M.-H. Chiu, L.-J. Li, Q.-H. Xu, G. Eda, S. A. Maier, A. T. S. Wee, C.-W. Qiu, and J. K. W. Yang, ACS Nano **12**, 1859 (2018).
29. W.-P. Guo, W.-Y. Liang, C.-W. Cheng, W.-L. Wu, Y.-T. Wang, Q. Sun, S. Zu, H. Misawa, P.-J. Cheng, S.-W. Chang, H. Ahn, M.-T. Lin, and S. Gwo, Nano Lett. **20**, 2857 (2020).
30. C. Li, X. Lu, A. Srivastava, S. D. Storm, R. Gelfand, M. Pelton, M. Sukharev, and H. Harutyunyan, Nano Lett. **21**, 1599 (2021).
31. H. Chen, V. Corboliou, A. S. Solntsev, D.-Y. Choi, M. A. Vincenti, D. de Ceglia, C. de Angelis, Y. Lu, and D. N. Neshev, Light: Sci. Appl. **6**, e17060 (2017).
32. N. Bernhardt, K. Koshelev, S. J. U. White, K. W. C. Meng, J. E. Fröch, S. Kim, T. T. Tran, D.-Y. Choi, Y. Kivshar, and A. S. Solntsev, Nano Lett. **20**, 5309 (2020).
33. Z. Liu, J. Wang, B. Chen, Y. Wei, W. Liu, and J. Liu, Nano Lett. **21**, 7405 (2021).
34. T. K. Fryett, K. L. Seyler, J. Zheng, C.-H. Liu, X. Xu, and A. Majumdar, 2D Mater. **4**, 015031 (2016).
35. T. Wang and S. Zhang, Opt. Express **26**, 322 (2018).
36. P. Hong, L. Xu, and M. Rahmani, "Dual bound states in the continuum enhanced second harmonic generation with Transition Metal Dichalcogenides monolayer," *Opto-Electron. Adv.* (to be published).
37. D. Li, C. Wei, J. Song, X. Huang, F. Wang, K. Liu, W. Xiong, X. Hong, B. Cui, A. Feng, L. Jiang, and Y. Lu, Nano Lett. **19**, 4195 (2019).
38. C. Qian, K. H. Choi, R. P. H. Wu, Y. Zhang, K. Guo, and K. H. Fung, Opt. Express **26**, 5083 (2018).
39. K. Guo, J. Wu, F. Chen, K. Zhou, S. Liu, and Z. Guo, Opt. Express **29**, 26841 (2021).
40. J. Ma, K. Guo, F. Chen, K. Zhou, S. Liu, and Z. Guo, Ann. Phys. **533**, 2100191 (2021).
41. S. Psilodimitrakopoulos, L. Mouchliadis, I. Paradisanos, A. Lemonis, G. Kioseoglou, and E. Stratakis, Light: Sci. Appl. **7**, 18005 (2018).
42. Y. Li, A. Chernikov, X. Zhang, A. Rigosi, H. M. Hill, A. M. van der Zande, D. A. Chenet, E.-M. Shih, J. Hone, and T. F. Heinz, Phys. Rev. B **90**, 205422 (2014).
43. H. H. Li, J. Phys. Chem. Ref. Data **9**, 561 (1980).
44. G. E. Jellison, Opt. Mater. **1**, 41 (1992).